Composites Part B 303 (2025) 112581

Contents lists available at ScienceDirect

Composites Part B

journal homepage: www.elsevier.com/locate/compositesb

Soft-hard self-alternating flexible organic-inorganic intercalated short-fiber mimetic bone lamellae

Mingyue Liu [a,1], Xiaoyu Han [b,1], Guilai Zuo [c], Pengcheng Xiao [b], Yue Zhao [d], Xiumei Mo [d,*], Juan Wang [a,**], Wenguo Cui [a,***]

[a] Department of Orthopaedics, Shanghai Key Laboratory for Prevention and Treatment of Bone and Joint Diseases, Shanghai Institute of Traumatology and Orthopaedics, Ruijin Hospital, Shanghai Jiao Tong University School of Medicine, 197 Ruijin 2nd Road, Shanghai, 200025, PR China
[b] Department of Rehabilitation Medicine, Key Laboratory of Physical Medicine and Precision Rehabilitation of Chongqing Municipal Health Commission, The First Affiliated Hospital of Chongqing Medical University, Chongqing, 400010, PR China
[c] Department of Orthopedic Oncology, The Affiliated Hospital of Qingdao University, Qingdao, 266000, PR China
[d] Department of Biomedical Engineering, Shanghai Engineering Research Center of Nano-Biomaterials and Regenerative Medicine, Donghua University, Shanghai, 201620, PR China

ARTICLE INFO

Keywords:
Electrospun
Bone lamellae
Multilayer structure
Short-fiber
Osteogenesis

ABSTRACT

Bone lamellae are the fundamental basis of bone structure and function. Simulating the multilevel ordered soft-hard alternating multilayer microstructures of these materials is extremely challenging. In this study, amorphous and highly structurally connected flexible inorganic silica nanofibers (SiO_2 NF) consisting of a network of silica-oxygen-silica bonds were prepared by sol-gel electrospinning and high-temperature calcination techniques, and highly entangled with organosodium alginate and hydroxyapatite nanoparticles (HAPs) to form soft-hard alternating structures wrapped in fixed-points by hydrogen bonding. Finally, soft-hard self-alternating flexible organic-inorganic intercalated short-fiber mimetic bone lamellae (ASH) were successfully constructed via the selective crystallization technique to adjust the temperature gradient for crystallization, thereby precipitating the intercalated structure. Based on the principles of crystal growth kinetics and solubility product equilibrium, ASH was transformed from a conventional disordered structure to a highly ordered multilayered soft-hard alternating structure with a porosity of up to 95 %. The ASH scaffold demonstrated exceptional shape memory properties, maintaining structural stability under 80 % strain and over 100 compression cycles. *In vitro* analyses revealed that sustained release of bioactive ions from ASH significantly enhanced osteogenic differentiation of bone marrow mesenchymal stem cells (BMSCs), as evidenced by upregulated expression of Fgf and Pdf/Flt4 genes. Furthermore, *in vivo* studies validated the scaffold's capacity to promote BMSCs recruitment and migration, thereby accelerating bone regeneration. In summary, mimetic bone lamellae were successfully constructed and accurately replicated the microstructure of natural bone lamellae, providing a new perspective and strategy for exploring the structure-function relationships of bone lamellae.

1. Introduction

In nature, organisms commonly employ soft-hard alternating structures to fulfill multiple functions, such as protection, support and flexibility. They are found in bones, teeth, shells, skin, plant stems, spider silk, and the raptorial appendages of mantis shrimp and wood [1,2]. For example, the soft-hard alternating structure of the mantis shrimp's raptorial appendages plays a crucial role for the penetration of hard objects [3]. Due to the soft-hard alternating structure of spider silk, it has extremely high strength and toughness, and its elasticity is maintained [4]. Notably, bones are composed of an organic matrix (primarily collagen) and inorganic minerals (primarily hydroxyapatite), forming an organic/inorganic composite soft-hard alternating structure at the microscale [5,6]. When fractures, osteoporosis, or bone defects occur,

* Corresponding author.
** Corresponding author.
*** Corresponding author.
E-mail addresses: xmm@dhu.edu.cn (X. Mo), juanwang1006@126.com (J. Wang), wgcui80@hotmail.com (W. Cui).
[1] The authors contributed equally to this work.

https://doi.org/10.1016/j.compositesb.2025.112581
Received 2 March 2025; Received in revised form 18 April 2025; Accepted 27 April 2025
Available online 28 April 2025

the soft-hard structures are disrupted, leading to limb deformities and functional impairments. For the clinical treatment of bone defects, the development of biomimetic matrices that can mimic the structure and composition of bone is therefore crucial. However, despite encouraging progress in mimicking bone structures in recent years, most studies still focus on designing disordered matrices structures [7–11]. Thus, developing novel matrices that can simulate both the hard mineral components and the soft organic matrix while precisely replicating the highly complex layered microstructure of natural bone tissue presents a formidable challenge.

Bone tissue serves as the quintessential dynamic load-bearing structure within the human body, and its optimal mechanical properties are typically derived from the harmonious integration of organic and inorganic components [12]. Inorganic components are composed of hydroxyapatite, which provides support and transmits external forces, whereas organic components are composed of collagen fibers, which effectively absorb and disperse energy [13]. This composite structure not only provides excellent mechanical properties to the lamellae but can also effectively regulate the cell biological behaviors. Therefore, to accurately replicate the natural organic-inorganic composite architecture of bone, various advanced technologies have been applied to the fabrication of biomimetic bone matrices, including phase separation [14,15], electrospinning [16–18], three-dimensional (3D) printing [19], sol-gel [20], self-assembly [21], and bio-3D braiding technologies [22]. Most existing scaffolds fail to replicate the multilayered soft-hard alternation and organic-inorganic intercalation of natural bone lamellae, leading to suboptimal mechanical stress conduction and osteogenic regulation. Sun et al. assembled hybrid interlaced scaffolds with nanoscale interfacial integration through nanoscale organic/inorganic interaction bonding to promote bone regeneration [23]. Additionally, Xie et al. prepared a porous organic/inorganic composite scaffold composed of bioglass and PLGA-collagen-gelatin nanofibers by electrospinning to promote bone regeneration [24]. Despite advancements in the fabrication of organic/inorganic nanofiber composite scaffolds, the mechanical stress conduction performance and bone regeneration capacity of these scaffolds are limited due to the excessive rigidity of inorganic nanofibers; effective promotion of bone regeneration could not be achieved by soft-hard self-alternating organic/inorganic intercalated structures. Inorganic nanofibers in conventional scaffolds are overly rigid, impairing shape memory and dynamic load adaptation. Therefore, the development of simple and effective strategies to prepare simulated natural bone lamellae with excellent osteogenic properties remains a challenge.

The development of biomimetic bone scaffolds faces significant challenges in simultaneously achieving mechanical robustness and biological functionality. Current approaches often struggle with fundamental trade-offs: highly mineralized scaffolds provide adequate strength but lack the porosity for cell infiltration, while soft polymeric structures offer biocompatibility but insufficient load-bearing capacity. Additional limitations include difficulties in replicating bone's hierarchical organization, accommodating dynamic remodeling processes, ensuring concurrent vascularization, and maintaining clinical scalability. As the basic functional unit in bone tissue regeneration and repair, the bone lamella plays a crucial role because of its exquisite soft-hard alternating lamellar structure [25]. To recapitulate the lamellar architecture of native bone tissue, Chen et al. developed biomimetic hierarchical hydrogel scaffolds featuring precisely organized multilayered concentric circular structures using a free-form injection fabrication approach [26]. However, the lack of interconnected porous channels in the ordered microstructures limited the cell signaling. In addition, Teng et al. prepared multilayered dense structured scaffolds based on the collagen fiber bundle structure of tendons *via* the mineralization technique [27]. However, the unidirectional array bundles of collagen layers could not achieve organic/inorganic intercalated structures. This occurred because existing techniques rely mainly on bottom-up stacking strategies. Bottom-up stacking strategies often lack interconnected porosity (<80 %) and bioactive ion release, hindering cell signaling and vascularization. Phase separation techniques facilitate the precise engineering of biomaterials with tunable lamellar architectures, tailored surface characteristics, and controlled mechanical properties through systematic optimization of processing conditions and parameters [28]. However, scaffolds prepared by a single-phase separation technique lack soft-hard alternating structures that are insufficient to accurately mimic the complex structure of bone lamellae. Notably, the soft-hard alternating lamellar structure affects the distribution and release of cytokines, which in turn regulate bone metabolism and remodeling processes [29–31]. Therefore, accurately simulating the multilayered ordered structure of soft-hard alternating laminae in bone lamellae to regulate cellular behaviors is the key to promoting bone regeneration.

Building upon the multilayered hierarchical porous architecture of native bone lamellae, novel soft-hard self-alternating flexible organic-inorganic intercalated short-fiber mimetic bone lamellae were meticulously constructed by combining flexible SiO_2 NFs at fixed points on the surfaces of sodium alginate and HAPs through sophisticated intermolecular hydrogen-bonding interactions and advanced selective crystallization techniques (Scheme 1A). ASH's soft-hard alternating multilayers (95 % porosity) mimic natural bone lamellae, enabling mechanical resilience (96 % shape recovery after 100 cycles) and nutrient diffusion. Flexible SiO_2 nanofibers and HAPs create a hydrogen-bonded intercalated network (Scheme 1B), balancing elasticity (101.4 kPa compressive strength) and bioactivity (Ca^{2+}/SiO_4^{4-} release). The effects of the ASH on the osteogenic induction of BMSCs and the vascularization of mixed cells within the metatarsal bone were further assessed *via* an osteogenesis-related protein expression assay and fetal rat metatarsal bone tube formation assay. Transcriptome sequencing elucidated that ASH bidirectionally accelerated bone regeneration through the activation of the Notch proangiogenic pathway and positive regulation of the cell adhesion-induced osteogenic pathway. Finally, *in vivo* experiments have demonstrated that the soft-hard self-alternating multilayered ordered structure of ASH promotes bone regeneration by inducing osteogenic differentiation of osteoblasts and angiogenesis (Scheme 1C). In conclusion, the soft-hard self-alternating flexible organic-inorganic intercalated short-fiber mimetic bone lamellae, with the accurate replication of the natural bone lamellae microstructure innovatively developed in this study, provides a groundbreaking therapeutic strategy for bone regeneration.

2. Experimental section

2.1. Preparation of flexible inorganic SiO_2 nanofibres

Tetraethyl orthosilicate (TEOS, 10 g) was combined with phosphoric acid (H_3PO_4, 0.07 g) and deionised water (DW, 10 g) in a stoichiometric ratio and homogenised for 24 h to facilitate the forming of a uniform silica sol. In this system, H_3PO_4 acted as an acid catalyst to promote the hydrolysis and subsequent polycondensation of TEOS. At the same time, an aqueous solution of 10 wt% poly(vinyl alcohol) (PVA) was prepared. The resulting silica sol was then mixed with the PVA solution in a 1:1 mass ratio to obtain a homogeneous electrospinning precursor solution. This step was critical, as it involved the compatibility and interaction of two different materials and had a significant effect on the morphology and properties of the final nanofibers. The electrospinning process was conducted under optimized parameters as follows: A 20G needle was employed under an applied voltage of 20 kV, with a controlled solution flow rate of 1 mL/h. The nanofibers were collected on a nonwoven fabric substrate positioned at a fixed working distance of 20 cm from the spinneret. Subsequently, the as-spun nanofibrous membranes were subjected to thermal treatment in a muffle furnace (FP310C, Yamato, Japan) with a controlled heating rate of 5 °C/min up to 800 °C, followed by isothermal calcination for 2 h. The high-temperature calcination process was used to remove PVA while promoting the formation of the amorphous structure of the SiO_2 NFs to obtain flexible and pure SiO_2

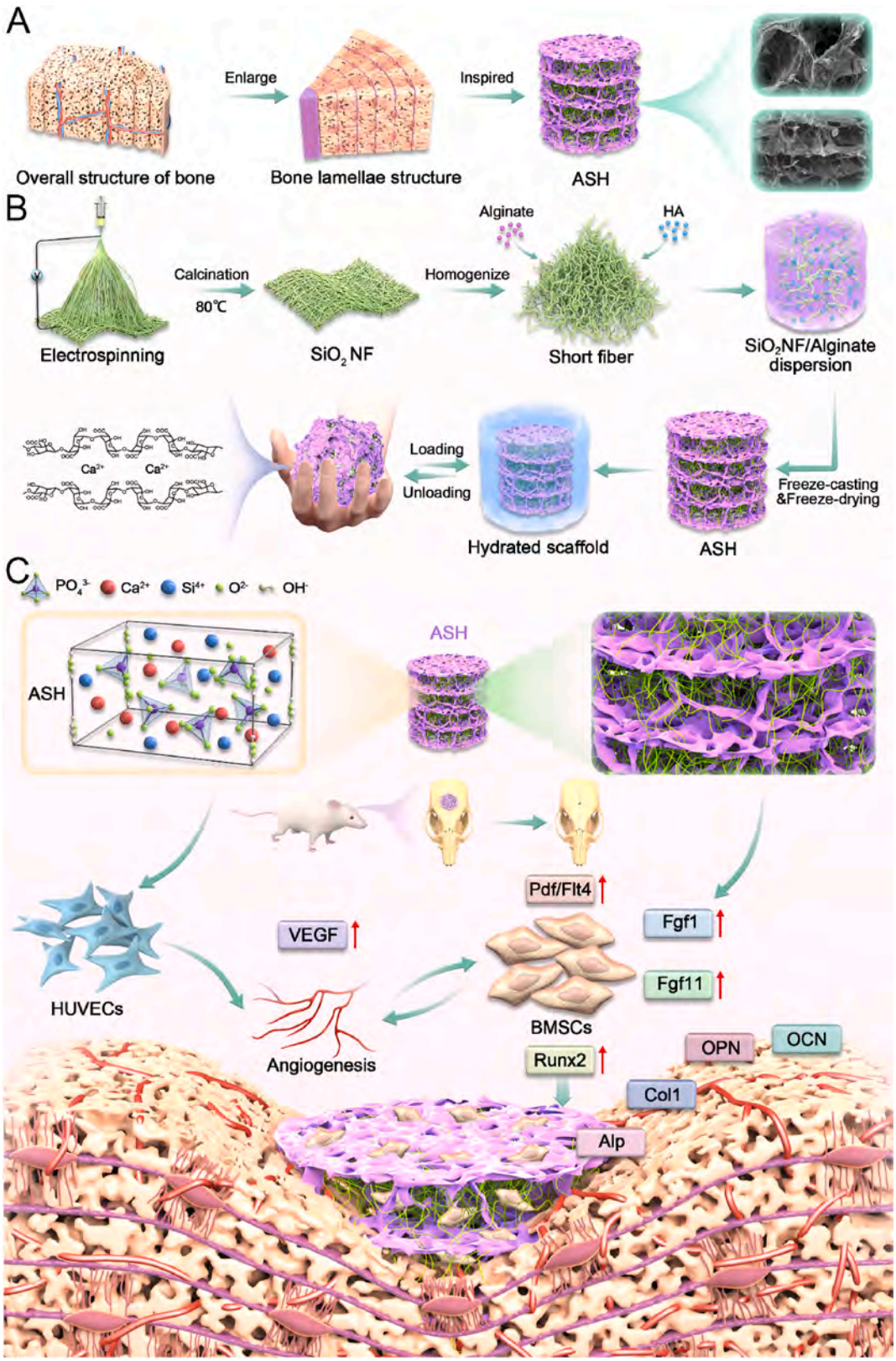

Scheme 1. Schematic diagram of the preparation and promotion of bone regeneration using a soft-soft self-alternating flexible organic-inorganic intercalated short-fiber mimetic bone lamellae. (A) Design of the mimetic bone lamellae inspired by natural bone structures. (B) Preparation process of the ASH. (C) ASH promoting vascular regeneration and directing stem cell differentiation to repair cranial defects in rats.

nanofiber membranes.

In this study, we used sodium alginate (Aladdin, Shanghai, China) with a viscosity of 200 cps as the base material. First, 0.15 g of SiO_2 NFs, 0.35 g of sodium alginate, and different masses of HAPs were uniformly dispersed in 50 mL of DW. A uniformly distributed dispersion of each component was produced by high-speed homogenization at 14,000 rpm for 30 min. Next, we stirred the resulting dispersion at room temperature for an additional 30 min to further stabilize the mixture. The dispersion was then transferred into preprepared molds of various shapes and sizes. Gradient cooling was applied, and the process was as follows: the dispersion was frozen in a cryogenic environment at −20 °C for 3 h; and next, the dispersion was placed in a cryogenic environment at −80 °C overnight to promote scaffold structure formation. Freeze-drying was performed to obtain uncrosslinked ASH. To enhance the structural integrity and biological compatibility of the scaffolds, the freeze-dried ASH constructs were subjected to ionic cross-linking by immersion in a 0.3 M calcium chloride ($CaCl_2$) solution for 30 min. This treatment facilitated the formation of stable calcium-mediated bridges between alginate chains, thereby improving both mechanical stability and cytocompatibility. The cross-linked mimetic bone lamellae were obtained by freeze-drying again. Scaffolds with varying HAPs contents were created by adding 0 %, 10 %, and 20 % (wt/v) HAPs to the dispersion, referred to as AS, ASH-0.1, and ASH-0.2, respectively. Scaffolds made from sodium alginate solution without SiO_2 NFs or HAPs (with a constant solid mass ratio of 30 %) were denoted AL and used as controls. Detailed scaffold material characterisation methods are provided in the Supporting *Information*.

2.2. Biocompatibility of the mimetic bone lamellae

To systematically evaluate the cytocompatibility of ASH scaffolds, we conducted parallel co-culture studies with BMSCs and HUVECs. The scaffolds were precision-sectioned into 2 mm-thick slices, sterilized in 75 % ethanol for 24 h, and extensively rinsed with PBS to ensure optimal cell culture conditions. First, cell viability was quantified via live/dead staining (Invitrogen, L3224, USA) using calcein-AM (green fluorescence) to identify viable cells and propidium iodide (red fluorescence) to detect non-viable cells. Proliferation kinetics were measured through CCK-8 assays (Yeasen, China) following manufacturer specifications. To examine the adhesion pattern of BMSCs on the scaffolds, skeleton staining (Yeasen, China) was employed to observe the cell morphology. Detailed experimental protocols and additional methodological specifications are available in the Supporting *Information*.

2.3. Osteogenesis of the mimetic bone lamellae

This study systematically investigated the osteoinductive capacity of biomimetic bone lamellae scaffolds on BMSCs. BMSCs were initially seeded at the density of 4×10^4 cells/well in DMEM/F-12 medium and allowed to adhere for 24 h under standard culture conditions. To induce osteogenic differentiation, the growth medium was replaced with osteogenic induction medium supplemented with 10 mM β-glycerophosphate, 0.1 μM dexamethasone and 0.25 mM ascorbic acid to create a defined osteogenic microenvironment. The induction process was evaluated at 4, 7, and 14 days to observe the osteogenic differentiation of the BMSCs over time. At each time point, we performed alkaline phosphatase (ALP) staining and alizarin red staining (ARS) and detected the expression of osteogenesis-related proteins via immunofluorescence in BMSCs cultured on the mimetic bone lamellae.

ALP and mineralization staining and analysis: BMSCs were inoculated in 24-well plates. After 7 and 14 days of osteogenic induction, the cells were fixed with 4 % paraformaldehyde. ALP and ARS staining were subsequently conducted to observe and quantitatively analyze ALP activity and matrix mineralization. Immunofluorescence Assay: BMSCs were also inoculated in 24-well plates. After 14 days of osteogenic induction, the cells were washed three times with PBS and then fixed with 4 % paraformaldehyde. A 0.1 % Triton X-100 treatment was performed for 15 min, followed by a 1 % bovine serum albumin (BSA) blocking step for 30 min to reduce nonspecific binding. Afterward, incubation with the target primary antibody and fluorescent secondary antibody was performed to observe the expression of osteogenesis-related proteins, such as collagen type I (Col I) and osteopontin (OPN), in the BMSCs using confocal microscopy.

2.4. RNA sequencing analysis

Total RNA extraction was performed from BMSCs co-cultured with either AL or ASH-0.1 scaffolds using TRIzol™ reagent (Thermo Fisher Scientific, USA), followed by purification to ensure RNA integrity. High-throughput sequencing was conducted on the Illumina NovaSeq™ 6000 platform (LC-Bio, Hangzhou, China) employing paired-end 150 bp (PE150) sequencing chemistry. Raw sequencing reads were subjected to quality control filtering to generate high-confidence clean data, which were subsequently processed using R-based bioinformatics pipelines. Differential gene expression analysis identified statistically significant DEGs ($p \leq 0.05$, fold-change ≥ 2) between experimental groups. These DEGs underwent comprehensive functional characterization through: (1) Gene Ontology (GO) annotation to elucidate biological processes, molecular functions, and cellular components, and (2) pathway enrichment analysis using the Kyoto Encyclopedia of Genes and Genomes (KEGG) database to identify significantly regulated signaling pathways.

2.5. Angiogenesis of the mimetic bone lamellae

To test the angiogenesis of the mimetic bone lamellae, the main experiments included the cell scratch test, cell migration test, fetal rat metatarsal angiogenesis model test, immunofluorescence test, and angiogenesis test. Detailed experimental protocols and additional methodological specifications are available in the Supporting *Information*.

2.6. Animal experimentation

2.6.1. Modeling and detection of the cranial defects in rats

In this study, we first sterilized the AL and ASH-0.1 scaffolds (2 mm thick and 5 mm in diameter) to ensure aseptic conditions for the experiments. Next, 6-week-old SD rats were selected as experimental animals and anesthetized via an intraperitoneal injection of sodium pentobarbital. Under anesthesia, we created a standardized defect model with a diameter of 5 mm in the cranium of each rat. The rats were then randomly divided into two groups, with sterilized AL and ASH-0.1 implanted into the cranial defects, to assess the effects of these scaffolds on cranial defect repair. Additionally, a blank control group was established; in this group, no treatment was applied to the cranial defect.

Postoperatively, all rats received routine husbandry management. At 6 and 12 weeks post-surgery, the rats were euthanized using an overdose of pentobarbital sodium solution to collect cranial bone samples. The collected skull samples were first fixed in 4 % PFA and then scanned using micro-CT. The scanning parameters were set to 65 kV, 100 μA current, and 120 μm resolution. The image data obtained from the micro-CT scans were quantitatively analyzed using SkyScan image analysis software, CTAn 1.14; the focus of this software is primarily on bone density. Bone mineral density (BMD) and the bone volume/total volume (BV/TV) ratio were used to evaluate the effects of material implantation on cranial defect repair at different time points.

2.6.2. Histological and immunofluorescent analyses

Following micro-CT analysis, the tissue samples were immersing in decalcification solution at 37 °C for one month to ensure complete decalcification. This step was crucial for histological analysis and facilitated subsequent sectioning and staining. After decalcification, the

tissue samples were dehydrated in graded alcohol, embedded in paraffin, and cut into 5 μm thick sections. Next, we stained the sections using hematoxylin-eosin (H&E) staining and Masson's trichrome staining to assess new bone formation 12 weeks after surgery. The tissue sections were then incubated with primary antibodies (CD31/α-SMA, OPN/OCN) for 1 h at room temperature, followed by washing with PBS to remove unbound antibodies. Afterward, the sections were incubated with the corresponding secondary antibody for 1 h at room temperature to detect specific antigen-antibody complexes. The signal intensity was quantified using ImageJ software.

2.7. Statistical analysis

All experiments were performed with a minimum of three independent replicates. Quantitative data are expressed as mean ± standard deviation (SD). For comparisons between two groups, statistical significance was determined using unpaired two-tailed Student's t-tests. Multiple group comparisons were analyzed by one-way analysis of variance (ANOVA) followed by Tukey's honestly significant difference post hoc test. A probability value (p) of less than 0.05 was considered statistically significant for all analyses.

3. Results and discussion

3.1. Preparation and characterization of the mimetic bone lamellae

To accurate replication of the natural bone lamellae microstructure, the soft-hard self-alternating flexible organic-inorganic intercalated short-fiber. bone lamellae were innovatively constructed. Specifically, HAP is the main inorganic component of human bone and was selected as the performance-modifying component for the ASH because of its excellent biocompatibility, osteoinductive properties, ease of modification, and good mechanical properties [32,33]. Firstly, the SiO_2 NFs was prepared using electrospinning and sol-gel methods [17]. Secondly, SiO_2 NFs, HAP, and sodium alginate were combined to create a homogeneous dispersion through high-speed homogenization, which ensured the uniform distribution of components in the solution and facilitated the formation of a porous structure. Thirdly, the prepared dispersion was poured into a mold, and after two freeze-drying processes and chemical cross-linking with a calcium chloride solution, a novel soft-hard self--alternating flexible organic-inorganic intercalated short-fiber mimetic bone lamella was successfully synthesized (Fig. 1A and B). The design of this scaffold exploited the principle of phase separation induced by water crystallization, where the phase separation of sodium alginate and SiO_2 NFs occurred during cryogenic freezing to form a layered porous structure, which endowed the mimetic bone lamella with shape memory functionality. The initial shape of the mimetic bone lamella was concealed in a temporary shape that could revert to the original form under appropriate stimuli. As shown in Fig. 1C and D, ASH recovered its initial shape in aqueous solution in 10–15 s, and the process can be recycled many times, which indicates that ASH has excellent shape memory properties (movie s1). The ASH scaffold's unique shape memory capability stems from an innovative triple-network design combining dynamic alginate chains, a SiO_2 nanofiber framework, and HAP nanoparticle interlocking. This sophisticated architecture enables temporary deformation through reversible ionic bond dissociation in the calcium-crosslinked alginate matrix, while the covalently-bonded silica network and HAP surface interactions provide the restoring forces to recover the original configuration.

Supplementary video related to this article can be found at https://doi.org/10.1016/j.compositesb.2025.112581

Furthermore, the surface morphology of the ASH was examined using scanning electron microscopy (SEM) and environmental scanning electron microscopy (ESEM). SEM images showed that all scaffolds presented a fibrous porous structure composed of randomly oriented fibers, closely resembling the natural extracellular matrix (ECM). (Fig. 1E). Notably, the cross-sectional structure of the mimetic bone lamella containing SiO_2 NFs displayed a unique soft-hard alternating multilayer structure with organic-inorganic intercalation (Supplementary Fig. S1). The integration of flexible inorganic SiO_2 NFs transformed the ASH from a conventional hydrogel architecture into a biomimetic ECM mesh fiber structure with organic-inorganic intercalation. Temperature gradient crystallization was regulated using a selective crystallization technique to achieve gradual crystallization of solutes and solvents.

At a specific low temperature, the water molecules initially formed columnar crystals, whereas the insoluble solute of SiO_2 NFs was preferentially excluded from the edges of the ice crystals and uniformly dispersed. As the temperature continued to decrease, sodium alginate and the functional ingredient HAPs gradually precipitated in an orderly manner between the neighboring ice crystals. Under the influence of hydrogen bonding, sodium alginate molecules became tightly bound to the surface of the short-fiber, and a dense encapsulation layer was formed. This process further increased the porosity and complexity of the hierarchical gradient structure of the mimetic bone lamella. The two-stage temperature gradient protocol (−20 °C for 3 h followed by −80 °C overnight) was meticulously developed to achieve three critical objectives in scaffold fabrication. First, the initial −20 °C phase (0.5–1 °C/min cooling rate) enables controlled ice nucleation that preserves bioactive component integrity while establishing directional crystal growth for aligned porosity formation. Second, the subsequent −80 °C phase ensures complete solvent crystallization while maintaining essential hydrogen bonding networks between SiO_2 nanofibers and alginate matrix, achieving optimal porosity preservation. Third, this specific gradient uniquely replicates native bone's lamellar spacing (3–7 μm) while maintaining exceptional HAP nanoparticle distribution uniformity. This optimized approach overcomes key limitations of conventional freeze-drying methods by simultaneously ensuring structural precision, bioactive preservation, and mechanical robustness - three factors essential for functional bone regeneration.

Additionally, energy spectral analysis and semi-quantitative detection revealed that elements such as carbon, oxygen, silicon, calcium and phosphorus were uniformly distributed on the surface of the mimetic bone lamella. The semiquantitative analysis indicated no significant difference in the silicon content among the AS, ASH-0.1, and ASH-0.2 containing SiO_2 NFs. However, the phosphorus content in the ASH-0.2 was greater than those in the other groups (Fig. 1G). The pore size of the mimetic bone lamella gradually decreased as the HAP content increased (Fig. 1F). High porosity not only facilitated the transport of the cellular nutrients and waste but also promoted the cell proliferation and migration [34]. As shown in Fig. 2D–F, the porosities of the AL, AS, ASH-0.1, and ASH-0.2 increased from 63 % ± 3 %–93 % ± 2 % as the HAPs content increased from 0 % to 20 % (Fig. 1H). These results further confirmed that the incorporation of HAPs and inorganic short-fiber successfully provided the mimetic bone lamellae with multilayered and porous structural features.

Furthermore, the mimetic bone lamella was analyzed by comprehensive infrared spectroscopy and thermogravimetric analysis to assess their chemical structure and thermal stability. Firstly, fourier transform infrared spectroscopy analysis revealed characteristic absorption peaks of the SiO_2 NF at 802 cm^{-1} and 1051 cm^{-1}; these peaks corresponded to the stretching vibration of the Si–O (Si–O–Si) bond. These results confirmed the successful preparation of the SiO_2 NFs and characterization of their chemical structure. The sodium alginate hydrogel showed a hydroxyl (O–H) stretching vibration at 3400 cm^{-1}, along with an absorption peak at 1650 cm^{-1} associated with the trans conformation of the carboxyl group (COO^-) (Fig. 2A). These characteristic peaks highlighted the chemical structure of sodium alginate and its role in the mimetic bone lamella. Additionally, X-ray diffraction analysis (Fig. 2B) indicated that the HAPs in the ASH-0.1 and ASH-0.2 exhibited characteristic peaks at $2\theta = 32°$. Based on these results, it was confirmed that the HAPs were successfully incorporated into the mimetic bone lamellar

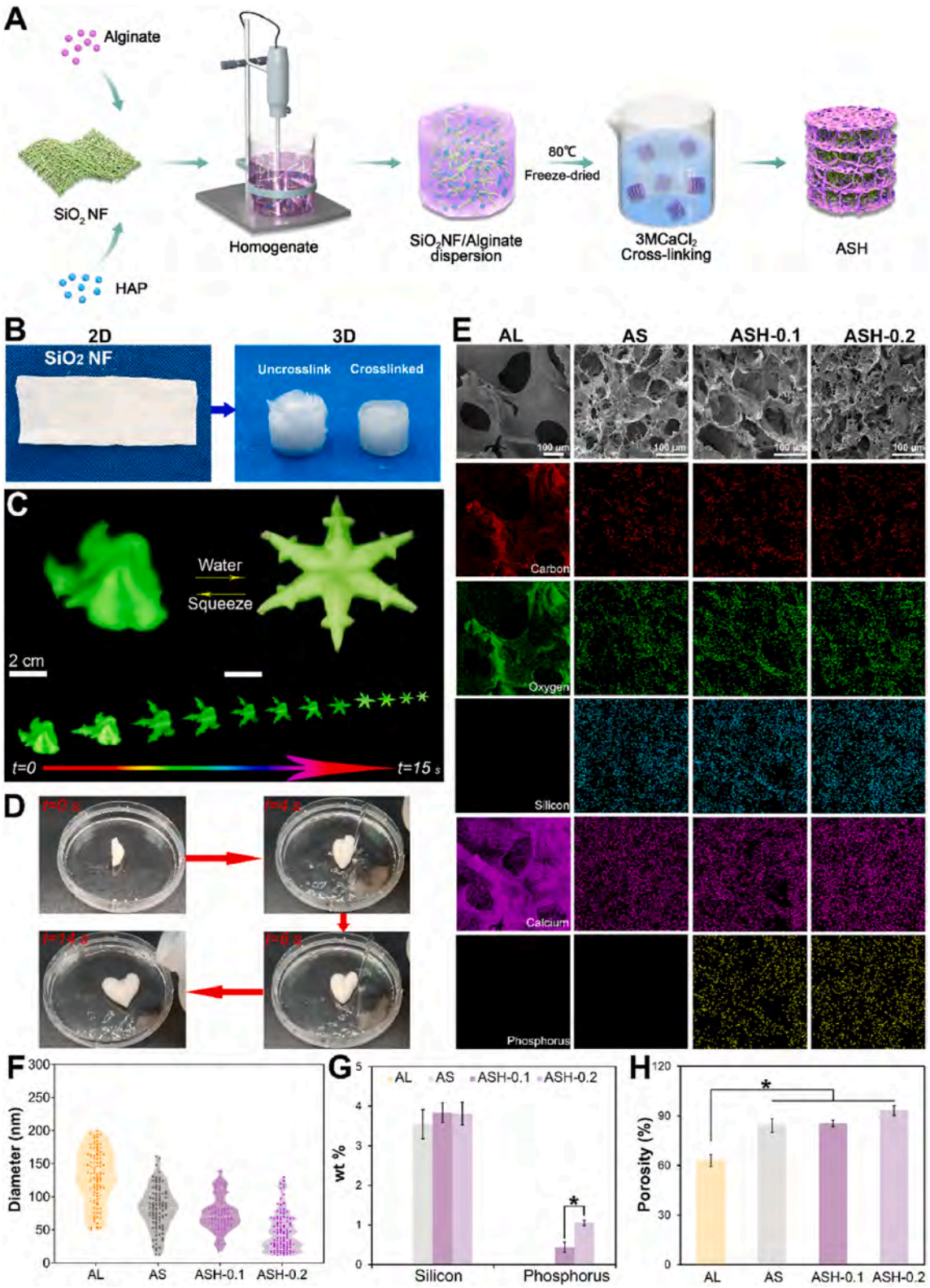

Fig. 1. Morphological characterization of the mimetic bone lamellae. (A) Preparation process of the ASH. (B) Optical image of the 2D inorganic SiO_2 NF membrane incorporated into the ASH. (C) Optical image depicting the shape recovery process of the snowflake-like ASH following water absorption. (D) Digital camera images demonstrating the shape memory properties of the heart-shaped ASH. (E) SEM images and elemental mapping of the ASH (Carbon: red, Oxygen: green, Silicon: blue, Calcium: purple, Phosphorus: yellow). (F, G) Pore size distribution of the ASH and semiquantitative analyses of silicon and phosphorus. (H) The statistical analysis of the porosity for the different ASH. Two-way ANOVA with Tukey's post hoc test, n = 3, * indicates $p < 0.05$. (For interpretation of the references to colour in this figure legend, the reader is referred to the Web version of this article.)

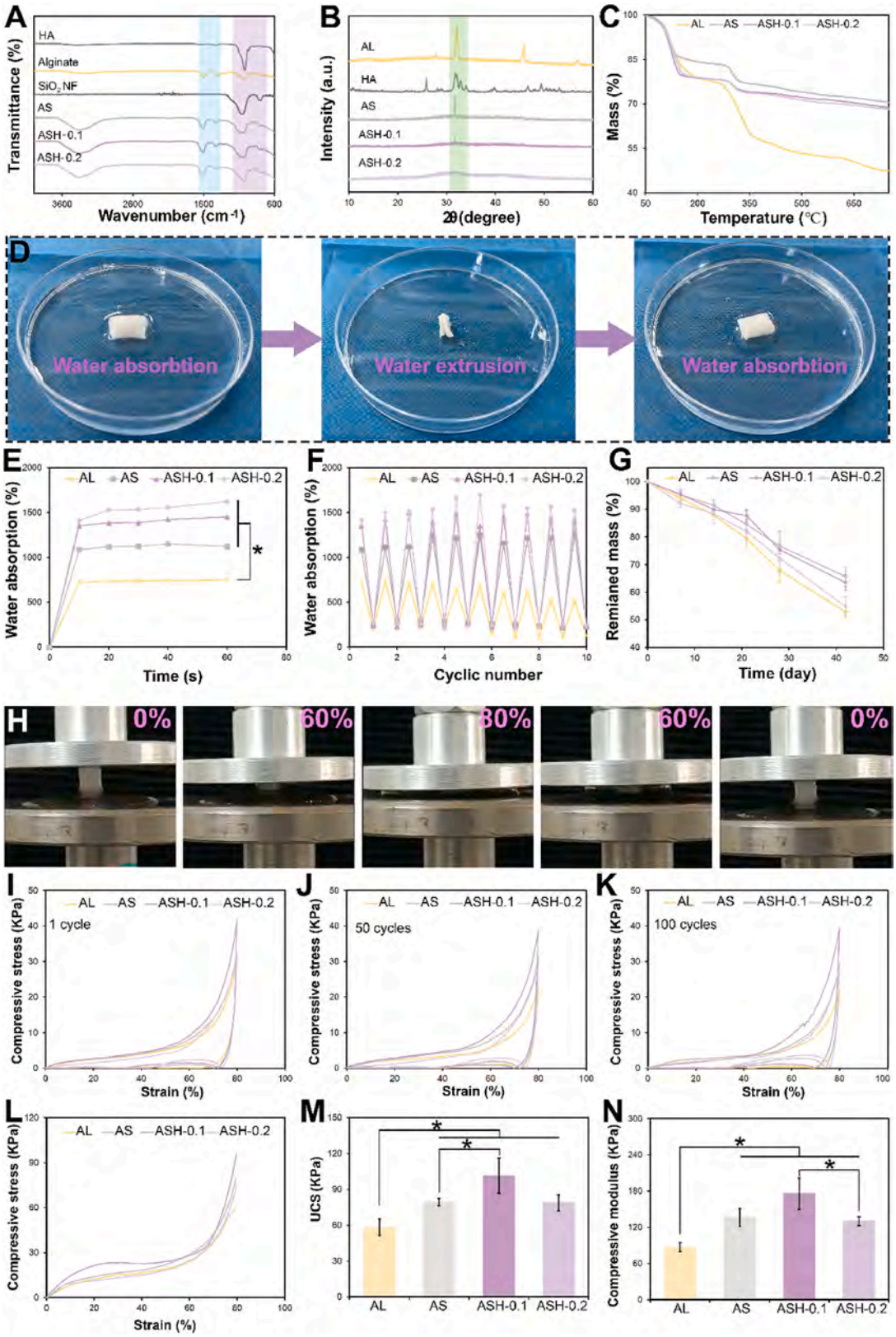

Fig. 2. Physicochemical characterization of the mimetic bone lamellae. FTIR (A) and XRD (B) analyses of the scaffolds with varying HAPs contents, along with TGA (C) to assess the thermal stability properties of each group. (D) Optical images of the water absorption properties of the ASH taken with a digital camera. (E–F) Quantitative analysis of water absorption in the ASH and the changes observed over 10 cycles. (G) Assessment of the degradation rate of the ASH over 6 weeks in vitro. (H) Macrostructural changes in the ASH during compression and shape recovery in aqueous media. (I–K) Stress-strain curves for the different scaffolds in the wet state after 1 cycle, 50 cycles, and 100 cycles. (L) Compressive stress-strain curves, (M) maximum compressive strength (UCS), and (N) compressive modulus of the ASH under dry conditions. Two-way ANOVA with Tukey's post hoc test, n = 3–4, * indicates $p < 0.05$.

materials while maintaining their crystal structure. The thermal stability of the mimetic bone lamella was assessed by thermogravimetric analysis. Fig. 2C shows the weight loss of the mimetic bone lamella with respect to the temperature. The weight of the HAPs remained relatively stable throughout the temperature increase, indicating good thermal stability. In contrast, the weight loss of the scaffolds occurred in three stages: 0°C–150 °C, 290°C–320 °C, and 320°C–650 °C. In the ranges of 0°C-150 °C and 250°C-350 °C, the weight loss was more rapid, likely caused by the release of moisture and volatile components. Above 350 °C, the rate of weight loss gradually decreased; these results indicated that the mimetic bone lamella began to reach a thermally stable state. Ultimately, above 600 °C, more than half of the weight of the AL was lost, whereas only 30 % of the weight of the mimetic bone lamella containing inorganic short-fibers (AS, ASH-0.1, and ASH-0.2) was lost. These results indicated that incorporating inorganic short-fiber significantly improved the thermal stability of the mimetic bone lamella.

The wettability and water absorption of the mimetic bone lamella is one of the key factors for cell survival. The high-water absorbency of the mimetic bone lamella is conducive to providing the necessary nutrient conditions for cell proliferation and differentiation. The experimental results revealed a significant increase in water absorption with increasing HAPs content. Specifically, as shown in Fig. 2D–F, the water absorption of ASH-0.2 was higher than that of AL (749 % ± 96 %, $p = 0$), AS (1122 % ± 111 %, $p = 0$) and ASH-0.1 (1451.82 % ± 35 %, $p = 0.00119$), with a statistically significant difference between the groups. Notably, the mimetic bone lamella reached near-maximum water absorption in less than 1 min of immersion, and a maximum water absorption of 1621 % was achieved (Fig. 2E). Furthermore, the water absorption remained almost constant after 1 min of absorption, indicating that the water absorption behavior of the scaffolds rapidly reached equilibrium in the initial period. After 80 % compressive deformation was applied to the mimetic bone lamella after water absorption, approximately 1000 % of the water was extruded. Upon repeating the compression and immersion operations ten times, the scaffold groups containing only short-fiber (AS, ASH-0.1, and ASH-0.2) rapidly absorbed water and returned to their initial morphology (Fig. 2F). The results of the water absorption test proved that the porous structure of the mimetic bone lamella fibers facilitates the rapid entry and retention of water. Additionally, the increase in porosity was positively correlated with the improved water absorption performance. The high water absorption capacity not only enhanced the cell adhesion and growth but was also crucial for bone tissue regeneration [35,36]. Furthermore, the reversible water-absorbing properties of the mimetic bone lamella suggest the ability to retain water after implantation and promote efficient penetration of nutrients to maintain cell survival and differentiation.

The excellent water-absorbing properties of the aforementioned scaffolds are mainly due to their connected porous structure and high porosity, which facilitates water absorption and retention. In addition, even after multiple successive compressions, these scaffolds can 'remember' and quickly return to their original shapes, which may be mainly related to the water absorption and the elasticity of the scaffolds. In order to test this hypothesis, the compressive strength of the simulated bone plates was exhaustively tested to evaluate their mechanical properties in both dry and wet states. To simulate the wet environment accurately *in vivo*, the compressive mechanical properties of the scaffolds were measured, especially in the aqueous environment. The experimental results revealed significant differences in compression performance between the AL and ASH-0.1. The ASH-0.1 demonstrated excellent elasticity and recovered to its initial height after cyclic compression at 80 % strain (Fig. 2H). For further testing, the mimetic bone lamellae was subjected to wet compression at 80 % strain for 1 cycle, 50 cycles and 100 cycles. (Fig. 2I–K). Quantitative analysis showed that the ASH-0.1 scaffold has good elasticity and shape memory, recovering 96 % and 94 % of its original shape after 50 and 100 cycles of 80 % strain compression, respectively. This is superior to many reported scaffolds, such as those produced by electrospinning or 3D printing, which typically lack this toughness under cyclic loading. To visually demonstrate the shape recovery ability of the ASH-0.1, the compressed scaffold in water was immersed. Experimental video S1 recorded the rapid recovery of the ASH-0.1 to its original state in approximately 10 s. In addition, the mimetic bone lamella was compressed to 90 % strain in the dry state and the compression characteristics were recorded (Fig. 2L). The maximum compressive strength of ASH-0.1 reached 101.4 ± 14.6 kPa; this value was significantly greater than that of AL (58.3 ± 6.8 kPa), AS (79.3 ± 3.0 kPa), and ASH-0.2 (78.8 ± 6.5 kPa) (Fig. 2M). Similarly, ASH-0.1 presented the highest value of the compression modulus (Fig. 2N). ASH-0.1 has the highest mechanical properties because a 10 % HAP content provides the desired reinforcement without impairing flexibility, while higher HAP contents (e.g. 20 % in ASH-0.2) can lead to brittleness. Due to these properties, ASH-0.1 is a highly promising candidate for bone tissue engineering.

3.2. Cytocompatibility of the mimetic bone lamellae

In bone tissue engineering, biocompatibility is the primary criterion for assessing the performance of bone scaffold materials since it directly affects the interaction between the materials and host cells and tissues [37]. Mimetic bone lamellae are flexible organic and inorganic composites made from short-fiber and essential for clinical applications. To comprehensively evaluate the biocompatibility of the mimetic bone lamellae, several experimental methods were used. *In vivo* live-dead fluorescence staining experiments were performed to visually assess the survival of BMSCs after 4 days of co-culture with AL, AS, ASH-0.1 and ASH-0.2. The results showed that although there was some cell death, the majority of cells maintained good morphology and viability. These scaffolds therefore support cell survival. Notably, the cell proliferation rate in the HAPs-containing ASH-0.1 and ASH-0.2 groups was significantly higher than that in the AL and AS groups (Fig. 3A). These results indicate that the addition of HAPs promotes cell proliferation. To further quantify cell proliferation, the proliferation of BMSCs on days 1, 4 and 7 was analyzed using the cell counting kit-8 (CCK-8) (Fig. 3B). The results aligned with the live-dead fluorescence staining findings. Initially, no significant difference was observed in the effects of the different scaffolds on cell proliferation. However, after four days of coculture, the cell densities in the ASH-0.1 and ASH-0.2 scaffold groups were significantly greater than those in the AL and AS groups; these results further confirmed the good cytocompatibility of the ASH-0.1 and ASH-0.2 scaffolds. Additionally, the skeletons of BMSCs co-cultured with the four sets of scaffolds were also stained on day 4 to observe cell morphology (Fig. 3C). After 4 days of culture, no significant difference was observed in the cell adhesion and spreading among the groups; these results indicated that all scaffolds supported cell adhesion and growth. Confocal microscopy images revealed the infiltration of BMSCs into the different scaffolds. Although BMSCs primarily aggregated on the surface of AL, variations in their penetration depths were observed in the nanofiber-containing AS, ASH-0.1, and ASH-0.2. Notably, the highest cell density and deepest penetration were observed in the ASH-0.1 (Fig. 3D), likely due to the porous structure and suitable porosity of the ASH-0.1. In summary, the results from live-dead fluorescence staining, CCK-8 proliferation analysis, backbone staining, and confocal microscopy demonstrated that the ASH exhibited good biocompatibility and supported the adhesion, proliferation, and penetration of BMSCs. These properties are crucial for the application of bone scaffold materials in bone tissue engineering and provide strong support for the effective repair and regeneration of bone defects.

3.3. Osteogenesis of the mimetic bone lamellae

In the field of bone tissue repair and regeneration, the efficient progression of the bone repair process depends on a precisely regulated cascade of biological events. This process is typically divided into three

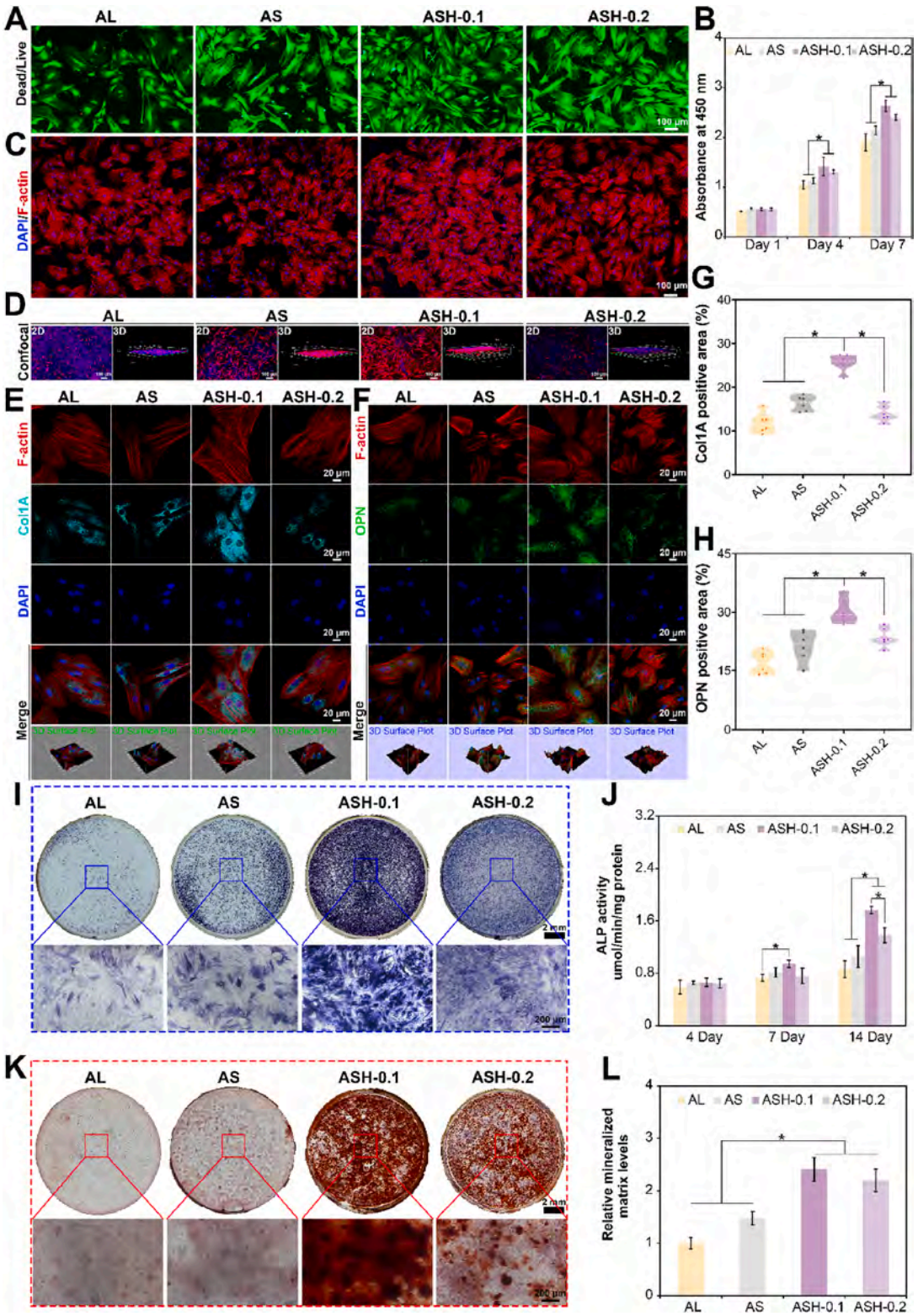

Fig. 3. Assessments of the in vitro biocompatibility and osteogenic differentiation properties of the mimetic bone lamella on BMSCs. (A) Survival/death fluorescence staining analysis of the BMSCs after coculture with the different scaffold groups (AL, AS, ASH-0.1, and ASH-0.2); live: green, dead: red. (B) CCK-8 determination of the cell proliferation rate of the BMSCs after 1, 4, and 7 days of coculture. (C) Observation of the morphology of the BMSCs after 4 days of coculture with different scaffolds; Nuclei: blue, F-actin: red. (D) Laser confocal microscopy images for the assessment of the cell growth in the scaffolds. (E, F) Images of the immunofluorescence staining of BMSCs; COL1A: blue–green; OPN: green. (G, H) Graphs showing the statistical analysis of the fluorescence intensity. (I, J) ALP staining and quantitative analysis of ALP protein expression. (K) ARS staining of the BMSCs cultured in osteogenic medium supplemented with MCM. (L) Quantitative analysis of the ARS staining. Two-way ANOVA with Tukey's post hoc test, n = 3; * indicates $p < 0.05$. (For interpretation of the references to colour in this figure legend, the reader is referred to the Web version of this article.)

consecutive phases: the reaction phase, the repair phase, and the remodeling phase [38]. The initial reaction phase with the active participation of stem cells marks the beginning of anabolism laying the foundation for tissue repair [39]. Afterward, the rapid formation of cartilage tissue is crucial at the site of the bone defect. This formation not only provides early biomechanical stability to the broken bone but also facilitates a smooth transition to the osteogenic process [40]. The design of bioactive materials plays a critical role in promoting the interplay and interdependence of bone regeneration and osteogenic activities in this ongoing biological process. The softness and stiffness of the mimetic bone lamellae significantly impact the behavior of BMSCs, including cell adhesion, proliferation, differentiation, and ultimately, osteogenic capacity. Studies indicate that BMSCs are sensitive to the mechanical properties of the mimetic bone lamellae. Mimetic bone lamellae with appropriate softness and stiffness can better mimic the ECM environment and provide BMSCs with the essential physical and chemical signals to promote their osteogenic differentiation. To investigate this mechanism in depth, the focus was on validating and testing the osteogenic capacity of the mimetic bone lamellae and its molecular mechanisms. After induction using osteogenic medium, the expression levels

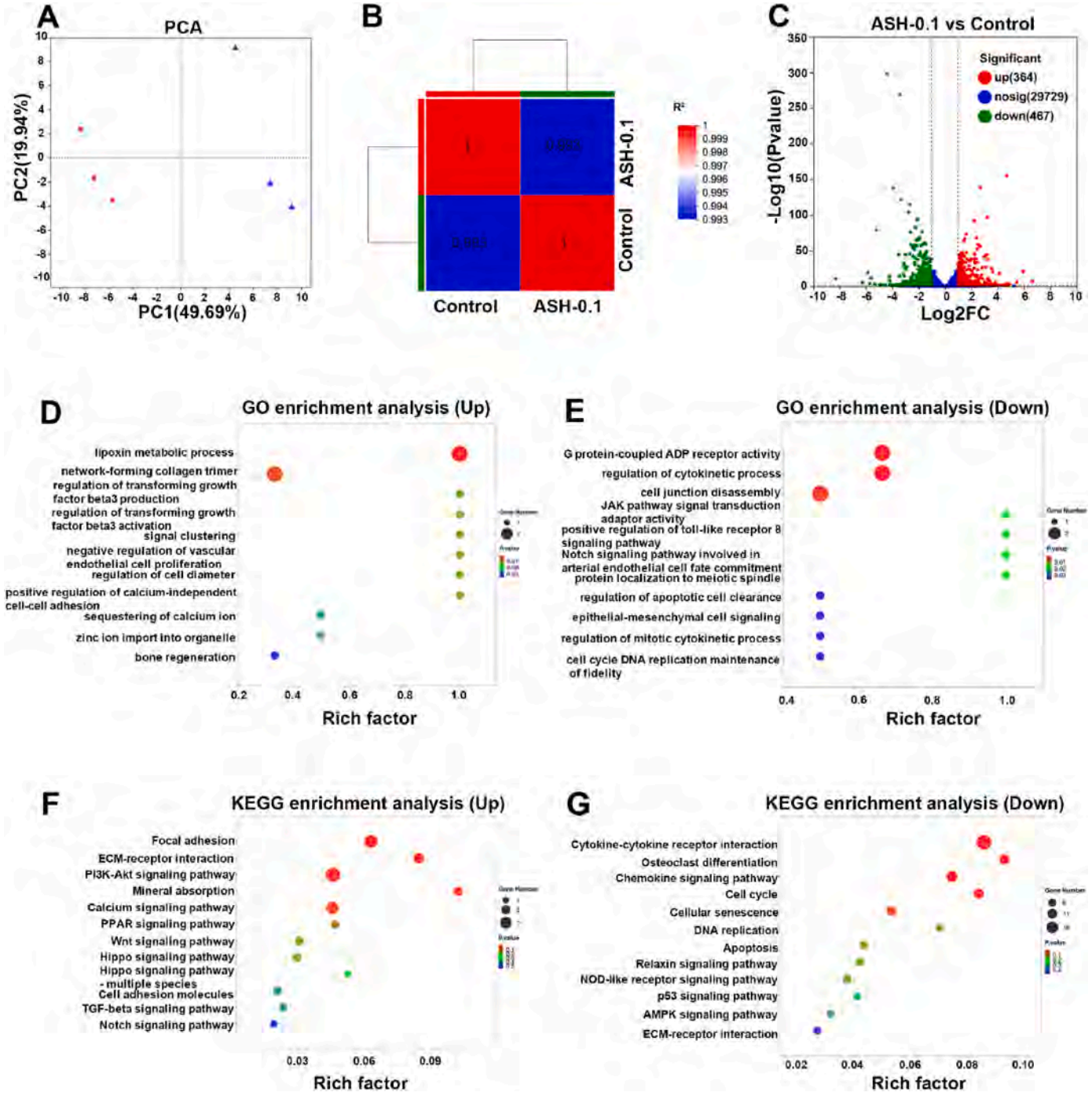

Fig. 4. Transcriptome sequencing analysis of the osteogenic capacity of the BMSCs induced by the ASH-0.1. (A, B) Sequencing of a total of 30,560 genes through transcriptome analysis, accompanied by PCA and correlation heatmap results. (C) Scatterplot indicating the expression changes of 831 differential mRNAs. (D, E) Gene Ontology enrichment analysis of the mRNA sequencing results showing that ASH-0.1 alleviated cellular stress and promoted the osteogenic differentiation of BMSCs. (F, G) KEGG enrichment analysis indicating that ASH-0.1 may directly or indirectly bind to protein ligands, activating the pro-vascular pathway.

of osteogenesis-related proteins in BMSCs co-cultured with the four groups of scaffold materials were measured using immunofluorescence assays at 7 and 14 days. In the immunofluorescence assay at 14 days, the intensity of the collagen type I (Col-I) protein was greater in the ASH-0.1 group than in the AL, AS, and ASH-0.2 groups (Fig. 3E). The same deduction was reached in the quantitative analyses (Fig. 3G). The high expression level of Col-I, which is a major collagen protein in the bone matrix, indicated the bone-enhancing efficiency of the mimetic bone lamellae. Similarly, consistent results were obtained for osteopontin (OPN) in the immunofluorescence experiments after 14 days of coculture (Fig. 3F–H). The elevated expression of OPN, which is a protein closely related to the mineralization process, further confirmed the osteogenic differentiation ability of the BMSCs in the ASH-0.1 group.

Moreover, alkaline phosphatase (ALP) and alizarin red staining (ARS) was performed on BMSCs after 14 days of co-culture with the four groups scaffolds. The marked variation in ALP staining intensity (Fig. 3I), a well-established biochemical marker of early osteogenic differentiation, quantitatively demonstrated the differential osteoinductive capacity of the various scaffold formulations on BMSCs. Both the staining intensity and the results from the quantitative analysis of the ALP protein expression indicated that the ASH-0.1 had the most pronounced osteogenic induction effect. Notably, the expression of ALP in the ASH-0.2 group was slightly lower than that in the ASH-0.1 group, possibly due to the amount of HAPs (Fig. 3J). Excessive HAPs potentially hindered the osteogenic differentiation of the cells, indicating that an appropriate amount of HAPs doped in the scaffolds was crucial for this process. Furthermore, ARS staining revealed that the size and number of mineral nodules in the ASH-0.1 group were significantly greater than those in the other groups (Fig. 3K–L). These results indicated that calcium deposition was most efficient in BMSCs cultured with the ASH-0.1. Therefore, the osteogenic differentiation of BMSCs could be effectively promoted by precisely regulating the softness and bioactive components of the scaffolds. The ASH-0.1 exhibited the best osteogenic induction effect because of its optimal HAPs content and softness.

To investigate the molecular mechanism by which the ASH-0.1 scaffold promotes the osteogenic differentiation of BMSCs, two separate RNA sequencing experiments were performed: control group and ASH-0.1 group. A total of 30,560 genes were sequenced in the transcriptome. The results from principal component analysis (PCA) and the correlation heatmap revealed a good distribution of relative expression abundance, and differences were observed between groups but not within groups (Fig. 4A and B). Our analysis identified a total of 831 DEGs between the two groups, including 364 upregulated genes and 467 downregulated genes. These findings indicated that ASH-0.1 significantly altered the gene expression (Fig. 4C). The up-down regulated DEGs were further analyzed through GO enrichment. The upregulated genes were significantly enriched in the pathways related to network-forming collagen trimers, regulation of transforming the growth factor beta3 production, positive regulation of the calcium-independent cell adhesion, and bone regeneration, among others (Fig. 4D). These results indicated that the introduction of ASH-0.1 promoted the activation of osteogenesis-related pathways in BMSCs. Additionally, the GO enrichment results for the downregulated DEGs revealed that pathways such as JAK pathway signal transduction adaptor activity, positive regulation of the toll-like receptor 8 signaling pathway, and cell junction disassembly showed increased enrichment factors; thus, the ASH-0.1 alleviated the cellular stress (Fig. 4E). Furthermore, KEGG enrichment analysis revealed significant enrichment of proangiogenic pathways, including the notch signaling pathway, wnt signaling pathway, and hippo signaling pathway, in the set of upregulated genes (Fig. 4F). These results indicated that ASH-0.1 could bind to protein ligands, activating pro-vascular pathways either directly or indirectly. Moreover, KEGG enrichment analysis of the downregulated genes revealed a significant difference between cytokine-cytokine receptor interactions and ECM-receptor interactions; this result supported our deduction (Fig. 4G).

The ASH scaffold's ability to simultaneously activate the Notch pro-angiogenic pathway and cell adhesion-induced osteogenic pathway plays a pivotal role in bone regeneration. The Notch pathway drives angiogenesis by promoting endothelial cell migration and tubule formation (Fig. 6), ensuring vascularization—a critical step for delivering oxygen, nutrients, and osteoprogenitor cells to the defect site [41,42]. Additionally, Notch signaling in BMSCs upregulates osteogenic genes (e.g., Runx2), directly enhancing bone formation [43]. Concurrently, the scaffold's fibrous porous structure mimics the native ECM, facilitating BMSC adhesion via integrin-mediated binding. This triggers mechanotransduction pathways (e.g., Wnt, Hippo) that further promote osteogenic differentiation (Fig. 4D–F), as evidenced by elevated expression of Col-I and OPN (Fig. 3E–H). Clinically, the synergistic coupling of early vascularization (Notch) and sustained osteogenesis (adhesion signaling) addresses a major challenge in large bone defect repair [44]. By co-activating these pathways, the ASH scaffold not only enhances regeneration efficiency but also demonstrates significant translational potential, positioning it as a biomimetic breakthrough that outperforms conventional scaffolds in both structural and functional performance.

3.4. Angiogenesis of the mimetic bone lamellae

Early reconstruction of the vascular network is essential for the effective treatment of large bone defects. Rapidly restoring damaged vascular networks to ensure blood flow in cranial defect models is challenging under normal physiological conditions [44]. Therefore, developing materials that can induce angiogenesis is essential for the early vascularization of the regenerated bone tissue. Vascular regeneration not only supplies vital nutrients and oxygen to the bone tissue but also promotes the proliferation and differentiation of the osteoblasts through the secretion of various growth factors and cytokines. Additionally, the migration and proliferation of HUVECs are critical in the vascularization process [45]. The vascularization potential of bionic bone fragments is important to promote bone regeneration, and the cell proliferation, scratch test and migration test were chosen to assess the effect of the scaffold on HUVECs. Live-dead fluorescence staining was performed on HUVECs cocultured with the scaffolds on days 1, 4, and 7 using the same method as that used for the BMSCs. The results showed that most of the cells maintained good morphology and viability. The cell proliferation rate in the ASH-0.1 and ASH-0.2 groups was significantly greater than those in the AL and AS groups (Fig. 5A). Quantitative analysis further revealed that the viable cell area was significantly higher in ASH-0.1 than that of the other groups (Fig. S4). These findings were consistent with those from the CCK-8 experiments (Fig. 5D) and further confirmed the promotional effect of the mimetic bone lamellae on HUVECs proliferation. Endothelial cell migration is a key component of tissue repair [46]. The ability of the mimetic bone lamellae to induce cell migration was verified by performing scratch assay (two-dimensional migration) and transwell migration assay (three-dimensional migration). The results from the scratch assays indicated that the ASH-0.1 and ASH-0.2 groups had the highest cell migration rates (Fig. 5B–E). Transwell experiments further revealed that the migration rate of HUVECs in the ASH-0.1 group ($p < 0.05$) was significantly greater than those in the other groups and was followed by that in the ASH-0.2 group (Fig. 5C–F). Thus, inorganic ions released from the mimetic bone lamellae containing appropriate amounts of HAPs and SiO_2 NFs could significantly induce the proliferation and migration of HUVECs, effectively promoting angiogenesis.

Angiogenesis in bone is regulated by various cell types, including osteoblasts, stromal cells, and bone marrow components [47]. The blood vessels in metatarsal bones can form complex networks without exogenous angiogenic factor stimulation. Thus, these components are valuable models for assessing the effects of bioactive substances released from materials on the angiogenic process [48]. In the present study, it was investigated how inorganic ions in the scaffolds regulate the number and activity of osteoblasts, which in turn affects angiogenesis in the metatarsal bones of foetal mice. Metatarsal bones of day 17.5 embryonic

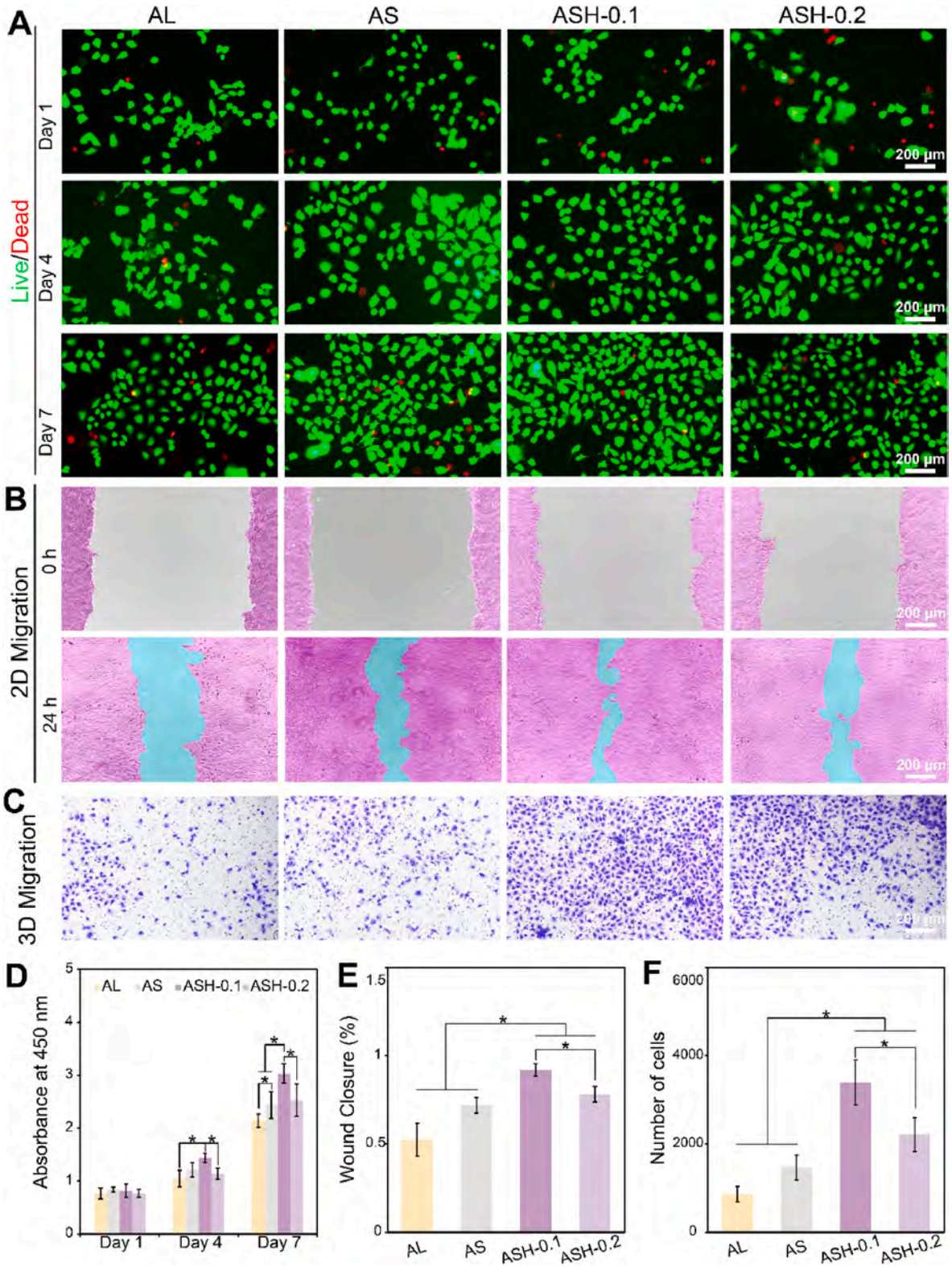

Fig. 5. Assessments of the in vitro biocompatibility and migration activity of the mimetic bone lamella on HUVECs. (A) Live/dead fluorescence staining analysis of HUVECs cocultured with different scaffold groups (AL, AS, ASH-0.1, and ASH-0.2) for 1, 4, and 7 days; live: green; dead: red. (B) Wound healing rate of the migrating cells in the wound scratch assay for HUVECs cultured in the extracts from the different scaffold groups (purple). (C) Cell migration assay using HUVECs stained with crystal violet. (D) CCK-8 quantification to assess the proliferation rate at corresponding time points. (E) Quantitative statistics of the number of migrating HUVECs. The data are expressed as the means ± SD, n = 3; * indicates $p < 0.05$. (For interpretation of the references to colour in this figure legend, the reader is referred to the Web version of this article.)

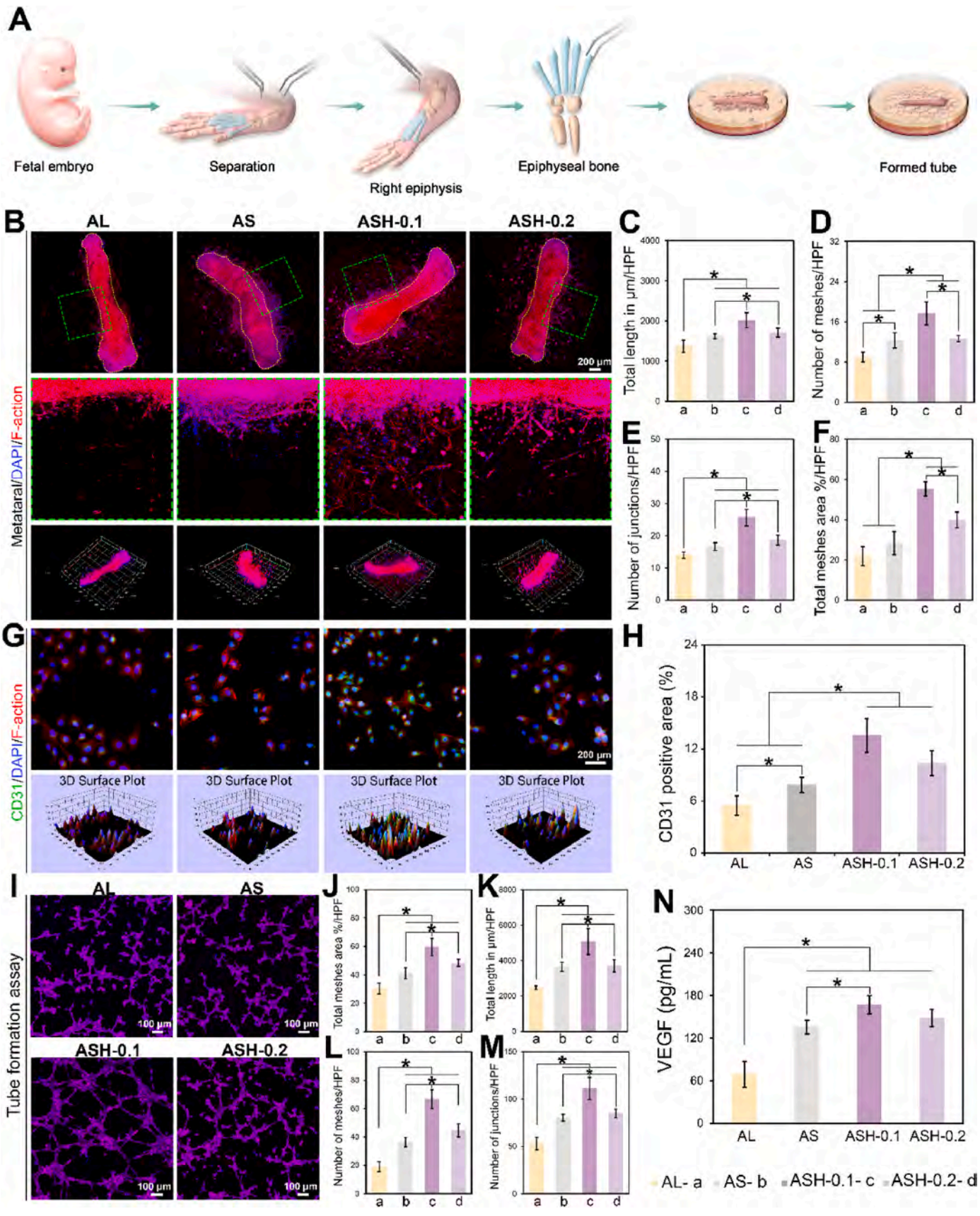

(caption on next page)

Fig. 6. Assessments of the mimetic bone lamella for in vitro angiogenic evaluation of HUVECs. (A) Schematic of the mouse fetal metatarsal bone stripping and graft angiogenesis culture model. (B) Confocal images of angiogenesis in mouse fetal metatarsal bones cocultured with the different scaffold extracts for 3 days. The results from the quantitative analyses included the total length of the hybrid cell-forming tubes (C), number of lattices (D), number of connections (E), and total lattice area (F). (G) Images of HUVECs stained with CD31 for immunofluorescence analysis; nucleus: blue; cytoskeleton: red; CD31: green. (H) Quantitative analysis of $CD31^+$ immunofluorescence intensity. (I) Confocal images of the blood vessel formation in HUVECs cocultured with different scaffolds for 24 h. Quantification includes the total length (C), number of grids (D), number of connections (E), and total grid area (F). (N) Quantification of VEGF produced by different groups of scaffolds cocultured with HUVECs. Two-way ANOVA with Tukey's post hoc test; * indicates $p < 0.05$ vs. AL. (For interpretation of the references to colour in this figure legend, the reader is referred to the Web version of this article.)

mice were first cultured in vitro on the surface of a matrix gel (Fig. 6A). During culture, endothelial cells formed tubular structures through mixed cell growth. Skeleton fluorescence staining and laser confocal microscopy revealed that the metatarsal bones presented significantly more blood vessel structures in ASH-0.1 containing HAPs and SiO_2 NFs (Fig. 6B). Additionally, increases in total tubule length, the number of connections, the number of lattices, and the total area of the lattices were also attained (Fig. 6C and D).

Simultaneously, co-culture of HUVEC with each group of scaffolds for 4 days was subjected to CD31 immunofluorescence staining. The results indicated that CD31 protein expression in the ASH-0.1 and ASH-0.2 groups was greater than those in the AL and AS groups (Fig. 6G). The results from the quantitative analysis of fluorescence intensity confirmed these observations (Fig. 6H). Notably, more tubes formation was observed in the ASH-0.1 and ASH-0.2 groups. These results were likely caused by the different amounts of HAPs in both scaffold groups since the bioactive ions they released effectively stimulated VEGF release; this accelerated tube formation and facilitated early vascularized bone repair (Fig. 6I). Quantitative analyses revealed that the total length of tubules, number of connections, number of grids, and total area of grids were greater in the ASH-0.1group than in the other groups (Fig. 6I–M). The results from the quantitative analysis of VEGF expression were similar (Fig. 6N). Overall, these findings indicated that ASH-0.1 significantly enhanced the vasculogenic ability of HUVECs by releasing bioactive ion.

3.5. *In vivo study of the mimetic bone lamellae for the treatment of large bone defects*

The development of bioactive scaffolds with improved osteogenic capacity is crucial for repairing bone defects. Designing biomimetic structures that mimic the natural composition and structure of bone is an effective strategy for developing these scaffolds [49–51]. HAPs are a major component of natural bone tissue, is osteoconductive and promotes cellular differentiation, facilitating the formation of new bone tissue. Based on these properties of HAPs, mimetic bone lamellae were constructed using the principles of crystal growth kinetics and solubility product balance. Their osteogenic function *in vivo* was further evaluated in a rat cranial defect model (Fig. 7). Three-dimensional reconstruction using micro-CT was performed at 6 and 12 weeks after scaffold implantation to directly observe the formation of new bone at the defect site. Cross-sectional and coronal assessments enabled the analysis of the 3D structure of the regenerated bone in detail. Micro-CT analysis at 12 weeks post-implantation (Fig. 7A) revealed distinct osteogenic outcomes across experimental groups: The negative control group demonstrated minimal new bone formation (BV/TV: 17.7 ± 1.6 %), while the AL scaffold group showed moderate but statistically significant osteogenesis (BV/TV: 27.1 ± 1.2 %, $p < 0.05$ vs control). Notably, the ASH-0.1 group exhibited substantially enhanced bone regeneration (BV/TV: 51.7 ± 2.0 %, $p < 0.01$ vs both control and AL groups), conclusively demonstrating the critical role of HAPs in accelerating the bone healing process through enhanced osteoconduction and osteoinduction (Fig. 7B). Bone mineral density (BMD) measurements (Fig. 7C) revealed that the ASH-0.1 scaffold group achieved superior mineralization (1.596 ± 0.055 g/cm^3) compared to both the negative control (1.125 ± 0.072 g/cm^3; $p < 0.001$) and AL scaffold groups (1.273 ± 0.047 g/cm^3; $p < 0.01$). This 29.2 % increase in BMD relative to the AL group and 41.9 % enhancement versus controls ($p < 0.01$ for both comparisons) provides compelling evidence of the ASH-0.1 scaffold's enhanced osteoconductive potential. In summary, the ASH-0.1 effectively mimicked the natural bone environment through its biomimetic structure and composition, providing suitable conditions for cell attachment and differentiation and thus significantly promoting bone regeneration.

3.6. *Histological and immunofluorescent analyses*

Histological analyses were performed and immunohistochemical techniques were used to assess the bone regeneration potential of the mimetic bone lamellae within 12 weeks in a rat model of cranial defects, and H&E staining and Masson's trichrome staining were performed on treated bone tissue from each group. This approach revealed the quality and maturity of the newly formed bone and was used to assess the degree of mineralization and collagen fiber arrangement (Fig. 7D and E). The results indicated that the defect area in the control group was predominantly filled with fibrous tissue, indicating limited new bone formation (Fig. 7D). In contrast, the AL group completely degraded within 12 weeks and exhibited some inward growth of new bone. The ASH-0.1 group demonstrated significant osteoconductive and osteoinductive properties, and new bone grew toward the interior of the scaffold and nearly filling the defect area by 12 weeks. The AL group experienced prolonged hypoxia in the center of the defect due to destruction of the vascular network and delayed reconstruction of the vasculature. This led to decreased cell viability and even tissue necrosis. However, the ASH-0.1 group provided an optimal environment for cell growth and proliferation because of its internal pore structure and fibrous multilayer design, thereby promoting greater new bone formation. Additionally, the ASH-0.1 group facilitated a favorable microenvironment for bone regeneration through the continuous release of calcium and silicon ions, combined with its layered fibrous porous structure. This structure not only supported cell adhesion and proliferation but also promoted angiogenesis and osteoblast differentiation, possibly through the release of biologically active substances such as silicon ions.

For immunohistochemical analysis, we performed immunofluorescence staining for the endothelial marker CD31 and the vascular smooth muscle marker α-SMA at 12 weeks. These experiments showed the effect of silicon ions released by ASH-0.1 on angiogenesis during bone repair. Compared with those in the blank control and AL groups, numerous CD31/α-SMA-positive vessels were present at the edges and centers of the defects in the ASH-0.1 group; thus, ASH-0.1 promoted angiogenesis (Fig. 7F). Quantitative analyses further confirmed this finding and showed that the areas positive for CD31 and α-SMA were significantly greater in the ASH-0.1 group than in the control and AL groups (Fig. 7H). Immunofluorescence staining for the osteoblast markers OPN and osteocalcin (OCN) was also performed. The expression levels of OPN and OCN were significantly greater in the ASH-0.1 group than in the control and AL groups, showing their effectiveness in promoting osteoblast differentiation and maturation (Fig. 7G). Quantitative analysis revealed that the areas positive for OCN and OPN were significantly greater in the ASH-0.1 group (Fig. 7H). In summary, through histological analysis and immunohistochemical techniques, we confirmed that the ASH-0.1 significantly promoted bone regeneration and angiogenesis.

In summary, while the ASH scaffold showed good osteogenic and angiogenic properties in rat cranial defects, it must be acknowledged

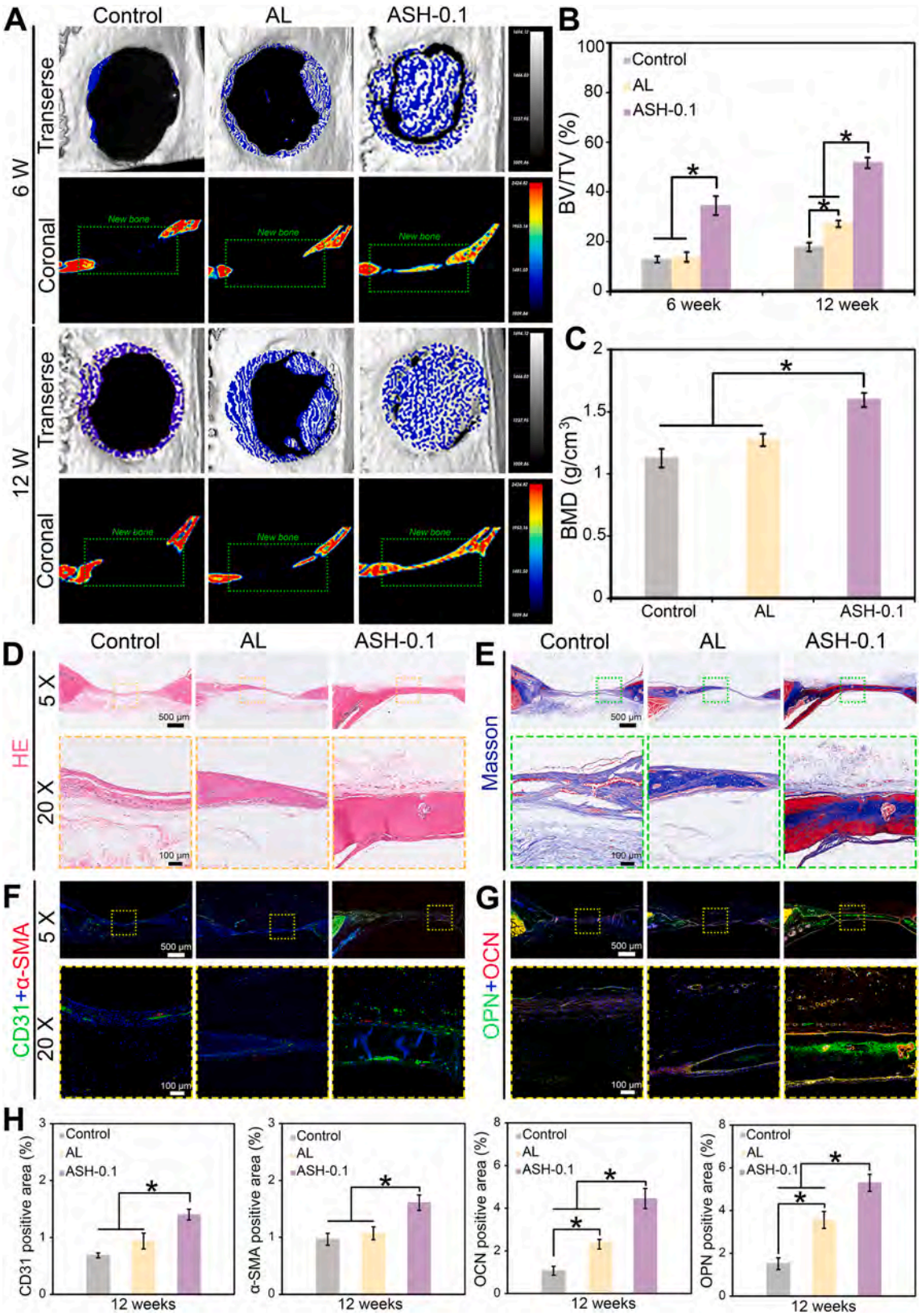

Fig. 7. Assessments of the mimetic bone lamella in a rat cranial bone defect model *in vivo* for up to 12 weeks. (A) Micro-CT images of the rat cranial bone defect model at different time points; blue areas indicate new bone. (B) Volume fraction of new bone in the cranial defect area at 6 and 12 weeks. (C) Bone mineral density in the cranial defect area at 12 weeks after surgery. H&E staining (D) and Masson's trichrome staining (E) were conducted on decalcified cranial bone tissue. Additionally, immunofluorescence staining of regenerated tissues was performed 12 weeks after surgery, revealing CD31 (green) and α-SMA (red) staining (F), as well as OCN (red) and OPN (green) staining (G). (H) Quantitative analysis of the positively stained areas was conducted using Image-Pro Plus software. The data are expressed as the means ± SD, n = 3; * indicates $p < 0.05$. (For interpretation of the references to colour in this figure legend, the reader is referred to the Web version of this article.)

that it has some limitations to guide future studies. First, its performance in large, load-bearing defects (e.g., segmental long bone defects) remains unvalidated, and mechanical properties may require further optimization for high-stress applications. Second, the 12-week study duration limits understanding of long-term scaffold degradation, inflammatory responses, and bone remodeling kinetics. Third, clinical translation faces challenges in scaling up production while maintaining the scaffold's intricate soft-hard microstructure and 95 % porosity, with sterilization methods and shelf-life stability yet to be addressed. Finally, the cell-free approach's efficacy in compromised healing environments (e.g., aged or diabetic models) remains unknown. To address these limitations, future research should focus on: (1) large animal studies using load-bearing defect models; (2) immunomodulation studies to optimise host responses; and (3) long-term (≥6 months) evaluations of bone maturation and mechanical recovery. These strategic directions will significantly advance the translational potential of the scaffold while addressing current research limitations in bone tissue engineering.

4. Conclusion

In this study, inspired by the multilayered hierarchical porous structure of natural bone lamellae, soft-hard self-alternating flexible organic-inorganic intercalated short-fiber mimetic bone lamellae were innovatively constructed. This structure featured a highly ordered soft-hard alternating multilayered fibrous porous design, effectively promoting bone defect regeneration by activating angiogenic and osteogenic signaling pathways. Due to the ordered structural and functional components, the mimetic bone lamellae had characteristics similar to natural bone, inducing directed osteogenic differentiation of stem cells and angiogenesis of endothelial cell through its soft-hard self-alternating structure and bioactive components significantly enhancing the formation of new bone tissue. In conclusion, the multilayered gradient soft-hard self-alternating flexible organic-inorganic intercalated short-fiber mimetic bone lamella prepared using selective crystallization techniques holds significant clinical potential for bone defect repair.

CRediT authorship contribution statement

Mingyue Liu: Writing – original draft, Methodology, Investigation, Formal analysis, Data curation, Conceptualization. **Xiaoyu Han:** Supervision, Resources, Formal analysis, Data curation. **Guilai Zuo:** Resources, Investigation. **Pengcheng Xiao:** Software, Data curation. **Yue Zhao:** Formal analysis, Data curation. **Xiumei Mo:** Writing – review & editing, Funding acquisition. **Juan Wang:** Writing – review & editing, Supervision, Resources. **Wenguo Cui:** Writing – review & editing, Methodology, Funding acquisition, Formal analysis.

Ethics approval and consent to participate

All animal procedures were approved by the Animal Ethics Committee of Shanghai Shengchang Biotechnology Co., LTD (the Ethical Clearance number is 2023-04-SGKYJS-CWG-045). All the authors were in compliance with all relevant ethical regulations.

Declaration of competing interest

The authors declare that they have no known competing financial interests or personal relationships that could have appeared to influence the work reported in this paper.

Acknowledgements

This research was supported by the National Natural Science Foundation of China (W2411085), China Postdoctoral Science Foundation (2023M742360, 2024M763902), China National Postdoctoral Program for Innovative Talents (BX20230228, BX20240454) and Science and Technology Commission of Shanghai Municipality (24YF2739500). The authors would like to express their gratitude to Edit Springs (https://www.editsprings.cn) for the expert linguistic services provided.

Appendix A. Supplementary data

Supplementary data to this article can be found online at https://doi.org/10.1016/j.compositesb.2025.112581.

Data availability

Data will be made available on request.

References

[1] Fang Y, Yang X, Lin Y, Shi J, Prominski A, Clayton C, Ostroff E, Tian B. Dissecting biological and synthetic soft–hard interfaces for tissue-like systems. Chem Rev 2022;122:5233.
[2] Zhang H, Ma Y, Wang Y, Niu L, Zou R, Zhang M, Liu H, Genin GM, Li A, Xu F. Rational design of soft–hard interfaces through bioinspired engineering. Small 2023;19:2204498.
[3] Patek SN, Korff WL, Caldwell RL. Deadly strike mechanism of a mantis shrimp. Nature 2004;428:819.
[4] Su I, Buehler MJ. Dynamic mechanics. Nat Mater 2016;15:1054.
[5] Liu Y, Luo D, Wang T. Hierarchical structures of bone and bioinspired bone tissue engineering. Small 2016;12:4611.
[6] Koons GL, Diba M, Mikos AG. Materials design for bone-tissue engineering. Nat Rev Mater 2020;5:584.
[7] Zhao R, Qian H, Zhu X, Zhang X, Chen Z, Yang X. Advancing osteoporotic bone regeneration through tailored tea polyphenols functionalized micro-/nano-hydroxyapatite bioceramics. Adv Funct Mater 2024;34:2401566.
[8] Chen R, Wang Y, Yu C, Zhang X, Wang Y, Yu T, Wu T. Bioactive glass-reinforced hybrid microfibrous spheres promote bone defect repair via stem cell delivery. Adv Fiber Mater 2025;7:240–53.
[9] Kong D, Wang Q, Huang J, Zhang Z, Wang X, Han Q, Shi Y. A biomimetic structural material with adjustable mechanical property for bone tissue engineering. Adv Funct Mater 2024;34:2305412.
[10] Zhu C, Pongkitwitoon S, Qiu J, Thomopoulos S, Xia Y. Tissue regeneration: design and fabrication of a hierarchically structured scaffold for tendon-to-bone repair (adv. Mater. 16/2018). Adv Mater 2018;30:1870116.
[11] Wang X, Tang M. Bioceramic materials with ion-mediated multifunctionality for wound healing. Smart Med 2022;1:e20220032.
[12] Reznikov N, Bilton M, Lari L, Stevens MM, Kröger R. Fractal-like hierarchical organization of bone begins at the nanoscale. Science 2018;360:eaao2189.
[13] Currey JD. Hierarchies in biomineral structures. Science 2005;309:253.
[14] Wang Z, Xiang Q, Tan X, Zhang Y, Zhu H, Pu J, Sun J, Sun M, Wang Y, Wei Q, Yu H. Functionalized cortical bone-inspired composites adapt to the mechanical and biological properties of the edentulous area to resist fretting wear. Adv Sci 2023;10:2207255.
[15] Cam-Hoa M, Hao-Yu C, Yi-Hsuan L, Amit Kumar S, Hsiang-Lin S, Yi-Sheng C, Kun-Ju L, Yu-Jung L, Hsing-Wen S. Engineering a biomimetic bone scaffold that can regulate redox homeostasis and promote osteogenesis to repair large bone defects. Biomaterials 2022;286:121574.
[16] Ryma M, Tylek T, Liebscher J, Blum C, Fernandez R, Böhm C, Kastenmüller W, Gasteiger G, Groll J. Translation of collagen ultrastructure to biomaterial fabrication for material-independent but highly efficient topographic immunomodulation. Adv Mater 2021;33:2101228.
[17] Liu M, Shafiq M, Sun B, Wu J, Wang W, El-Newehy M, El-Hamshary H, Morsi Y, Ali O, Khan AUR, Mo X. Composite superelastic aerogel scaffolds containing flexible SiO(2) nanofibers promote bone regeneration. Adv Healthc Mater 2022;11:e2200499.
[18] Xu Y, Saiding Q, Zhou X, Wang J, Cui W, Chen X. Electrospun fiber-based immune engineering in regenerative medicine. Smart Med 2024;3:e20230034.
[19] Yuan X, Zhu W, Yang Z, He N, Chen F, Han X, Zhou K. Recent advances in 3D printing of smart scaffolds for bone tissue engineering and regeneration. Adv Mater 2024;36:2403641.
[20] Maria Grazia R, Vincenzo G, Luigi A. Hybrid composite scaffolds prepared by sol–gel method for bone regeneration. Compos Sci Technol 2010;70:1861.
[21] Zhen Y, Bin W, Wei L, Xiaoke L, Kaini L, Zejun F, Jiao Jiao L, Yudi N, Zihao H, Hui L, Du W, Jianjing L, Yanan D, Jianhao L, Dan X. In situ self-assembled organoid for osteochondral tissue regeneration with dual functional units. Bioact Mater 2023;27:200.
[22] Xianrui X, Jiangyu C, Dan L, Yujie C, Chunhua W, Guige H, Thorsten S, Bernd R, Mohamed ELN, Hany ELH, Jia J, Xiumei M, Jinzhong Z, Jinglei W. Multiphasic bone-ligament-bone integrated scaffold enhances ligamentization and graft-bone integration after anterior cruciate ligament reconstruction. Bioact Mater 2024;31:178.
[23] Li X, Li Z, Wang P, Lu G, Tong L, Liu Q, Chen Y, Lin J, Luo E, Liang J, Jiang Q, Fan Y, Zhang X, Sun Y. Dopamine-Integrated nanointerface between fibrillar matrix and hydrophilic nanohydroxyapatite regulates immune microenvironment to boost endogenous bone regeneration. Adv Funct Mater 2023;33:2212738.

[24] Weng L, Boda SK, Wang H, Teusink MJ, Shuler FD, Xie J. Novel 3D hybrid nanofiber aerogels coupled with BMP-2 peptides for cranial bone regeneration. Adv Healthcare Mater 2018;7:1701415.
[25] Wegst UGK, Bai H, Saiz E, Tomsia AP, Ritchie RO. Bioinspired structural materials. Nat Mater 2015;14:23.
[26] Geng X, Tang Y, Yuan B, Dai Y, Yu H-P, Xiong Z-C, Zhu Y-J, Chen X. Biomimetically ordered ultralong hydroxyapatite nanowires-based hierarchical hydrogel scaffold with osteoimmunomodulatory and osteogenesis abilities for augmenting bone regeneration. Chem Eng J 2024;488:151136.
[27] Tao Y, Zhichao H, Zhenzhen W, Binxin X, Jiangchen L, Le F, Qinmei W, Yanshan L, Dongying L, Sangzhu T, Chuanzi L, Weichang L, Wei T. An engineered lamellar bone mimicking full-scale hierarchical architecture for bone regeneration. Bioact Mater 2023;27:181.
[28] Wang C, Liu P, Liu K, Su S, Cheng X, Wang Z. Study of the effect of layered structure on phase separation and heat transfer properties of phase change materials. J Energy Storage 2024;84:110705.
[29] Zhang L, Dong Y, Liu Y, Liu X, Wang Z, Wan J, Yu X, Wang S. Multifunctional hydrogel/platelet-rich fibrin/nanofibers scaffolds with cell barrier and osteogenesis for guided tissue regeneration/guided bone regeneration applications. Int J Biol Macromol 2023;253:126960.
[30] Kapur S, Baylink DJ, William Lau KH. Fluid flow shear stress stimulates human osteoblast proliferation and differentiation through multiple interacting and competing signal transduction pathways. Bone 2003;32:241.
[31] Mao J, Saiding Q, Qian S, Liu Z, Zhao B, Zhao Q, Lu B, Mao X, Zhang L, Zhang Y, Sun X, Cui W. Front cover: reprogramming stem cells in regenerative medicine (smart medicine 1/2022). Smart Med 2022;1:e38.
[32] Chun F, Jianmin X, Xiaopeng Y, Dong Z, Rongcai L, Meng Z, Lunguo X, Xiaoya W, Qingqiang Y, Jiang C, Chengtie W. Co-inspired hydroxyapatite-based scaffolds for vascularized bone regeneration. Acta Biomater 2021;119:419.
[33] Zhang Q, Ma L, Ji X, He Y, Cui Y, Liu X, Xuan C, Wang Z, Yang W, Chai M, Shi X. High-strength hydroxyapatite scaffolds with minimal surface macrostructures for load-bearing bone regeneration. Adv Funct Mater 2022;32:2204182.
[34] Pengfei X, Kunxi Z, Shifeng Y, Guifei L, Jingbo Y. Biomimetic, biodegradable, and osteoinductive Microgels with open porous structure and excellent injectability for construction of microtissues for bone tissue engineering. Chem Eng J 2021;414:128714.
[35] Mingxian L, Huanjun Z, Juan C, Shuangli L, Jianfang H, Changren Z. Chitosan-chitin nanocrystal composite scaffolds for tissue engineering. Carbohydr Polym 2016;152:832.
[36] Bhosale AM, Richardson JB. Articular cartilage: structure, injuries and review of management. Br Med Bull 2008;87:77.
[37] Lu Y, Zhang W, Wang J, Yang G, Yin S, Tang T, Yu C, Jiang X. Recent advances in cell sheet technology for bone and cartilage regeneration: from preparation to application. Int J Oral Sci 2019;11:17.
[38] Dimitriou R, Jones E, McGonagle D, Giannoudis PV. Bone regeneration: current concepts and future directions. BMC Med 2011;9:66.
[39] Claudia S, Heilwig F, Christian HB, Carsten R, Georg ND, Katharina S-B. The multifaceted roles of macrophages in bone regeneration: a story of polarization, activation and time. Acta Biomater 2021;133:46.
[40] Begam H, Nandi SK, Kundu B, Chanda A. Strategies for delivering bone morphogenetic protein for bone healing. Mater Sci Eng C 2017;70:856.
[41] Burger MG, Grosso A, Briquez PS, Born GME, Lunger A, Schrenk F, Todorov A, Sacchi V, Hubbell JA, Schaefer DJ, Banfi A, Di Maggio N. Robust coupling of angiogenesis and osteogenesis by VEGF-decorated matrices for bone regeneration. Acta Biomater 2022;149:111.
[42] Cackowski FC, Anderson JL, Patrene KD, Choksi RJ, Shapiro SD, Windle JJ, Blair HC, Roodman GD. Osteoclasts are important for bone angiogenesis. Blood 2010;115:140.
[43] Mao J, Saiding Q, Qian S, Liu Z, Zhao B, Zhao Q, Lu B, Mao X, Zhang L, Zhang Y, Sun X, Cui W. Reprogramming stem cells in regenerative medicine. Smart Med 2022;1:e20220005.
[44] Tong L, Liao Q, Zhao Y, Huang H, Gao A, Zhang W, Gao X, Wei W, Guan M, Chu PK, Wang H. Near-infrared light control of bone regeneration with biodegradable photothermal osteoimplant. Biomaterials 2019;193:1.
[45] Burger MG, Grosso A, Briquez PS, Born GME, Lunger A, Schrenk F, Todorov A, Sacchi V, Hubbell JA, Schaefer DJ, Banfi A, Di Maggio N. Robust coupling of angiogenesis and osteogenesis by VEGF-decorated matrices for bone regeneration. Acta Biomater 2022;149:111.
[46] Ponsen A-C, Proust R, Soave S, Mercier-Nomé F, Garcin I, Combettes L, Lataillade J-J, Uzan G. A new hemostatic agent composed of Zn2+-enriched Ca2+ alginate activates vascular endothelial cells in vitro and promotes tissue repair in vivo. Bioact Mater 2022;18:368.
[47] Cackowski FC, Anderson JL, Patrene KD, Choksi RJ, Shapiro SD, Windle JJ, Blair HC, Roodman GD. Osteoclasts are important for bone angiogenesis. Blood 2010;115:140.
[48] Song W, Fhu CW, Ang KH, Liu CH, Johari NAB, Lio D, Abraham S, Hong W, Moss SE, Greenwood J, Wang X. The fetal mouse metatarsal bone explant as a model of angiogenesis. Nat Protoc 2015;10:1459.
[49] Feng P, Zhao R, Tang W, Yang F, Tian H, Peng S, Pan H, Shuai C. Structural and functional adaptive artificial bone: materials, fabrications, and properties. Adv Funct Mater 2023;33:2214726.
[50] Lee SS, Du X, Kim I, Ferguson SJ. Scaffolds for bone-tissue engineering. Matter 2022;5:2722.
[51] Koushik TM, Miller CM, Antunes E. Bone tissue engineering scaffolds: function of multi-material hierarchically structured scaffolds. Adv Healthcare Mater 2023;12:2202766.